RESEARCH ARTICLE

The flow around a model helicopter main rotor in ground effect

N. D. Nathan · R. B. Green

Abstract Wind tunnel measurements of the wake below and ahead of a model helicopter main rotor in simulated forward flight in ground effect are presented. The wind tunnel used was equipped with a rolling road, and the ground speed was matched to the wind tunnel speed for a representative simulation in the wind tunnel of forward flight over the ground. Particle image velocimetry was used to investigate the structure of the wake, and it was observed that the moving ground had a remarkable effect on the flow; the wake is closer to the rotor and its size is reduced compared with the stationary ground case. The detailed distribution of vorticity within the wake is affected by the moving ground, and the mechanism for this is discussed in the paper.

1 Introduction

An isolated helicopter main rotor flow is characterised normally by an induced downflow through the rotor disk, and a wake consisting of persistent, inter-twined helical vortices travelling below the rotor. This wake is skewed backwards in forward flight. For a fixed wing aircraft, the vortex wake trails behind the aircraft, but for a helicopter, the vortices can remain in close proximity to the rotor disk and blades for lengthy periods, and the persistent presence of these vortices is a major cause of noise, vibration,

performance and handling issues unique to rotorcraft. The fluid dynamics of a rotor wake are rich with interesting phenomena and are a challenge for the experimentalist and computational fluid dynamicist alike. Of particular importance for experimental studies is the enormous spatial extent of the rotor wake and its unsteady nature, and particle image velocimetry (PIV) has become an indispensible tool along with other experimental measurement techniques. The testing environment requires particular care. Wind tunnel testing requires the use of large open test sections (e.g. Raffel et al. 2004), or where validation data for CFD are required, a closed wind tunnel test section with instrumented walls is best used (Raffel et al. 2011). This paper concerns the wake of a rotor in forward flight in ground effect and its investigation in a wind tunnel, and the correct simulation of the ground by a moving belt is shown to be the key feature of such an experiment.

A helicopter rotor is said to be in ground effect when the main rotor disk is less than a few disk diameters above the ground. The important parameter is the non-dimensional rotor height $\frac{h}{D}$, where h is the rotor height above the ground and D is the rotor diameter. The presence of the ground near the rotor has been known to alter its aerodynamics in ground effect (IGE) compared to out of ground effect (OGE), and this may impart beneficial effects on the performance of the rotor. For example, the main rotor power requirement is reduced for a given thrust setting when IGE. However, there are well-documented cases of handling and operational difficulties IGE (Key 1999). An important example of such a ground-effect-related operational difficulty is due to the formation of huge clouds of dust (or snow) around a helicopter that may form in appropriate conditions. The rotor wake lifts up loose matter off the

N. D. Nathan
Department of Mechanical Engineering,
National University of Singapore, Singapore, Singapore

R. B. Green (✉)
Aerospace Sciences Division, School of Engineering,
University of Glasgow, Glasgow, Scotland, UK
e-mail: Richard.Green@glasgow.ac.uk

ground, and this is swept up high into the flow field all around the helicopter. This may lead to a loss of pilot situational awareness, commonly referred to as brownout (or whiteout), and has been attributed to the loss of numerous aircraft. Such operational and performance issues IGE are ultimately associated with the important fluid dynamic effect of the ground on the structure of the wake below the rotor, and this is the subject of the present paper.

The most obvious difference in the wake of a hovering rotor IGE is the expansion of the wake instead of the notional contraction observed OGE. Smoke flow visualisation experiments conducted by Fradenburgh (1960) showed this expansion, and a schematic diagram is presented in Fig. 1. Velocity measurements identified the presence of a relatively stagnant zone of fluid in the central region of the expanding rotor wake. It is conceptually easy to observe that the presence of the ground plane near the vicinity of the rotor disk alters the trailing vortex wake, thus affecting the rotor slipstream and inflow velocities. Evidence for this is seen in experiments where the presence of the ground plane alters the axial and radial locations of the tip vortices trailed by the rotor (Light 1989). More recent PIV experiments conducted with a ground plane and rotor model have traced the variation in the tip vortex trajectories caused by varying rotor ground distances (Saritas et al. 2004), and an in-depth analysis of the tip vortex system of the wake of a rotor IGE hover was conducted by Lee et al. (2008) using flow visualisation and dual-plane PIV. The structural alterations to the wake of the rotor in turn have an effect on the thrust and power characteristics of the rotor, and this is where the majority of research into ground effect has been directed. Flight testing on helicopters and experimental testing on isolated rotor models have shown that the power required to hover IGE is significantly less than OGE at a given rotor thrust (Küssner 1937; Betz 1937; Knight and Hefner 1937; Zbrozek 1947; Fradenburgh 1960; Hayden 1976). Experimental research has shown these performance benefits to be affected by parameters such as blade loading (Zbrozek 1947), number of rotor blades, blade shape, blade twist and aspect ratio, for overview see (Leishman 2006). The inclination of the ground over which the rotor is hovering is also seen to change hover performance IGE (Fradenburgh 1960). Most substantially, the non-dimensional rotor height $\frac{h}{D}$ is seen to have the greatest influence on the rotor hover performance IGE. Mathematical analysis conducted by Küssner (1937) and Betz (1937) has shown most of the performance advantage IGE hover to be observed at ground heights up to half a rotor diameter above the ground, and related research has shown the rotor to lose most of the ground effect benefit as it reaches a distance of 1 rotor diameter

above the ground (Knight and Hefner 1937; Hayden 1976). Above this height, the rotor is considered to be OGE *from a performance point of view*.

Ground effect has also been seen to have substantial effects on the performance of a rotor in low-speed forward flight (in wind tunnel tests the wind tunnel–free stream velocity represents the flight speed of the helicopter). The advance ratio μ is a non-dimensional forward flight speed expressed as $\mu = \frac{V_\infty}{V_{\text{tip}}}$, where V_∞ is the forward flight speed and V_{tip} is the rotor tip speed relative to the rotor axis. The normalised advanced ratio $\mu^* = \frac{V_\infty}{V_h}$ uses the rotor hover-induced velocity $V_h = V_{\text{tip}}\sqrt{\frac{C_T}{2}}$ as the scaling velocity, where $C_T = \frac{T}{\rho A V_{\text{tip}}^2}$ is the rotor thrust coefficient and T, ρ and A are the rotor thrust, ambient fluid density and rotor disk area, respectively. This normalised advance ratio is a preferable parameter to use for the fluid dynamics as it accounts for the momentum imparted to the flow by the rotor disk. In forward flight, the rotor is travelling over a stationary ground. At low advance ratio, the wake fluid is pushed ahead of the rotor into the stationary air ahead, and the interaction between the rotor wake flow and the still air results in the formation of a flow separation line on the ground some distance upstream of the rotor. The rotor wake expanding along the ground rolls up to form a weak vortex as a result of this separation, and these features form nearer the rotor disk as the advance ratio of the rotor is increased. Saijo et al. (2003) observed that the separation point position oscillates at low frequency. Flow visualisation experiments conducted by Sheridan and Wiesner (1977) showed how this wake roll up was affected by advance ratio, and Fig. 3 shows a set of schematic diagrams based on their work. When the ground vortex forms ahead of the rotor disk, as seen in Fig. 3a and b, additional flow is induced through the rotor disk by the ground vortex system. Sheridan and Wiesner (1977) showed changes in the power required IGE forward flight compared with hover IGE. Their result is reproduced in Fig. 2. Power P initially increased in low-speed forward flight, and at a particular flight speed, the power required reached a maximum value close to the power P_{OGE} required by the rotor to hover OGE. At the point of maximum-induced inflow through the rotor, the power required was observed to be a maximum. Increasing the advance ratio further was seen to cause the ground vortex to form further downstream, behind the leading edge of the rotor disk, causing a degree of upflow through the disk, as shown in Fig. 3c. The power required by the rotor at this point is reduced and is seen to fall significantly below that required OGE. The presence of the ground-induced vortex in the wake has been documented to exist up to a forward flight speed equivalent to an advance

Fig. 1 Comparison between the OGE and IGE wake of a hovering rotor. The *figure* shows schematic diagrams of mean-flow particle pathlines. After Fradenburgh (1960). **a** Hover OGE, **b** hover IGE
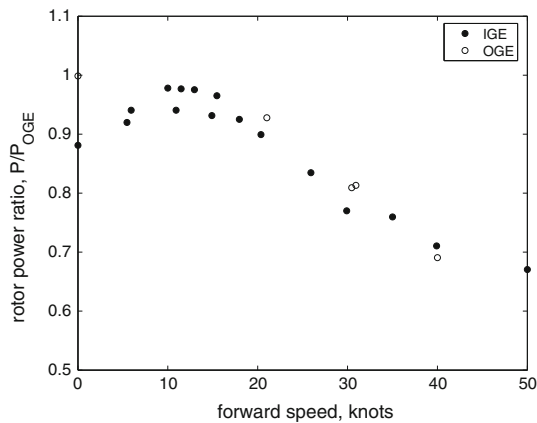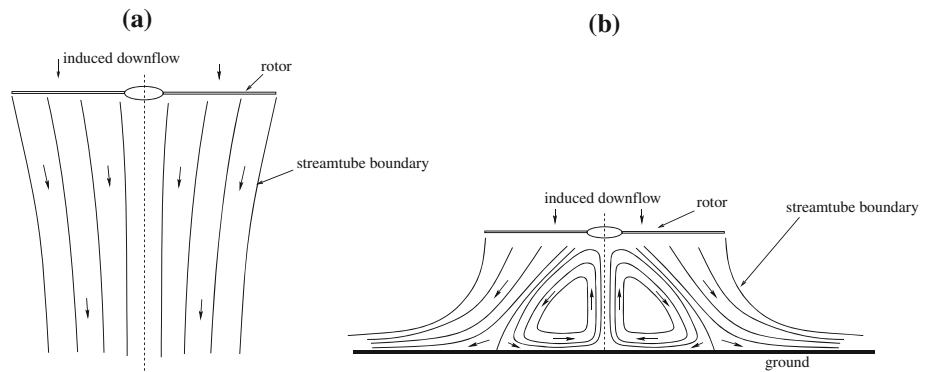

Fig. 2 Ratio of rotor power P for forward flight IGE to power required for hover OGE P_{OGE}. After Sheridan and Wiesner (1977)

Fig. 3 Schematic diagrams of the evolution of the ground effect wake in low-speed forward flight after Sheridan and Wiesner (1977). **a** Low advance ratio: wake rolls up some distance ahead of the rotor disk, **b** moderate advance ratio: recirculation system just ahead of the disk, **c** high advance ratio: ground vortex forms behind leading edge of disk

ratio of $\mu \approx 0.1$, beyond which it is not visible in the flow field (Leishman 2006). Flight operations IGE have been seen to require additional trim inputs, especially during the flight regimes where maximum power was required (Ganesh 2006). Research conducted by Curtiss et al. (1984, 1987) made use of an isolated rotor towed along a flat track in a long towing shed. This work established that the wake behaviour can be separated into two flow regimes known as the recirculation regime and the ground vortex regime. Classification of the wake was made on the basis of rotor to ground distance $\frac{h}{D}$ and the thrust normalised advance ratio μ^*. Dependent upon ground height, the recirculation regime tends to occur in the range $0.4 < \mu^* < 0.7$, and the ground vortex regime in the range $0.7 < \mu^* < 1.0$. In the recirculation regime, the wake roll up occurs ahead of the rotor, and some of the wake fluid recirculates through the rotor disk, while in the ground vortex regime, the wake roll up occurs below the rotor disk (corresponding to the caricature in Fig. 3c).

Interactions between the oncoming freestream and the rotorwake expanding along the ground plane ahead of the rotor have been seen to result in the formation of a horse-shoe-shaped boundary on the ground plane, some distance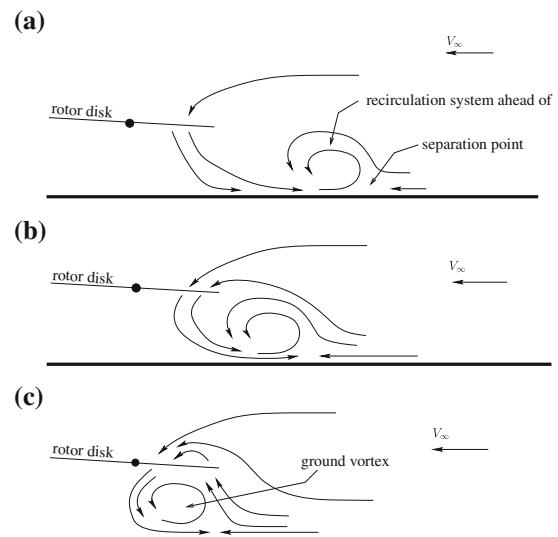 upstream from the rotor disk, and the location of this interaction boundary is determined by the advance ratio of the flow. Boyd and Kusmarwanto (1983) conducted a flow visualisation experiment using smoke and tufts on a fixed ground plane. PIV tests conducted by Ganesh et al. (2005) among others, using an isolated rotor model in a wind tunnel fitted with a static ground plane, identified the recirculation regime to be dominated by a recirculation loop (Saijo et al. 2003; Ganesh and Komerath 2004, 2006; Ganesh et al. 2005). Through these experiments, it was identified that the recirculation loop was characterised by 7–8 tip vortices re-directed back towards the rotor and re-ingested through it. Hot-wire anemometry studies conducted by Curtiss et al. (1984) reported large fluctuations in the wake during the recirculation regime flow field, although little lateral flow was observed in the flow field. Hot-wire measurements conducted by Ganesh and Komerath (2004), Ganesh et al. (2005) near the rotor disk plane also

showed the presence of fluctuations in the inflow near the rotor, which was measured to be 5–10% higher than that experienced OGE, and these fluctuations have been attributed to the ingestion of the tip vortices from the recirculation loop. Additional hot-film investigations along a vertical plane from the ground to the plane of the rotor disk, just ahead of the leading edge showed a highly unsteady flow field (Hanker and Smith 1985). These investigations were also used to measure changes in moments and forces affecting a model helicopter fuselage and tail rotor, during the ground vortex regime. Experiments conducted by Boer et al. (2001) were concentrated on a $0.7 \times 0.6R$ region of the flow field to investigate the ground vortex formed under the rotor disk, and PIV was used to identify changes to the location of the ground vortex cores for changing rotor ground distances and flight speeds. While information of the ground vortex was established through these experiments, details about the structure, size and strength of the ground vortex could not be determined from the data provided. PIV measurements of the ground vortex taken by Ganesh et al. (2005) showed the ground vortex to form with vorticity from the tip vortices trailed by the rotor blades and also showed the ground vortex strength to be more than four times that of the tip vortices (Ganesh 2006; Ganesh and Komerath 2006).

A major challenge with experimentation for forward flight of a model rotor close to the ground is how the ground is represented. The most realistic experimental model is for the rotor model to fly over a stationary ground; this is how (Curtiss et al. 1984, 1987) conducted their experiments, for which very large towing facilities were used. Wind tunnels offer a more convenient environment for experimentation. A moving belt to model the ground in a wind tunnel flow has been used in the past for fixed wing V/STOL aircraft (Turner 1966, 1967), and significant effects on the aerodynamics were observed under certain conditions for these flows. In a rotor ground effect experiment, (Boer et al. 2001) used a boundary layer control jet (tangential blowing) to vary the ground boundary layer height and did not observe a significant effect on the vortex core positions compared with other parameters such as wind tunnel speed. More recently, (Ganesh 2006) used a wind tunnel where the rotor was sitting over a stationary ground plate with the wind tunnel flow running past. They recommended for future work investigating the possible importance of accounting for the ground boundary layer, although it was also argued that it might not be that important as the strength of the ground vortex was very high relative to the ground boundary layer. The motivation for the present work was to investigate how an experimental model of ground effect on a rotor in forward flight can be performed in a wind tunnel, and this has been achieved through the use of a rolling road (moving belt) in

the wind tunnel to more correctly account for the rotor to ground relative speed in forward flight. Forward flight simulation of the rotor is achieved with the ground speed V_g set to the same speed and direction as the wind tunnel free stream V_∞. High-resolution measurements using PIV of the ground effect wake show that the effect of this moving ground boundary condition is to restructure the wake to a remarkable degree.

2 Experimental method

The experimental results presented in this paper are from tests conducted on a $D = 1$ m diameter, 4-blade rotor running in a low-speed, closed-return wind tunnel with a 2.7 m wide $\times$ 2.10 m high $\times$ 4 m long, octagonal working section. A moving ground (continuous belt moving over platen) comprised the lower surface of the working section, and PIV was used as the main experimental technique to investigate the rotor wake fluid dynamics. A schematic diagram of the experiment is shown in Fig. 4. The (r, y, z) axis system is indicated, where y is in the vertical direction, and r is the radial coordinate on the rotor disk parallel to the wind tunnel longitudinal axis pointing directly upstream. All the rotor components were derived from commercially available, radio-control, scale-model parts. A rotor requires trim in forward flight due to differential dynamic pressure on the advancing and retreating blades, and consequently a trim system was designed into the rotor. A feather hinge allowed for the blade collective (mean geometric angle of attack) and longitudinal and lateral cyclic pitch angles θ_{1s} and θ_{1c} to be altered, but the hub was rigid in flap and lag. Linear stepper motors (0.03 mm per step) connected to a swash plate were used to vary the cyclic pitch angles for trim inputs, and blade cyclic angles were determined using linear potentiometers attached to each stepper motor. A Panasonic 750 W digital servo AC motor powered the rotor system, and this also
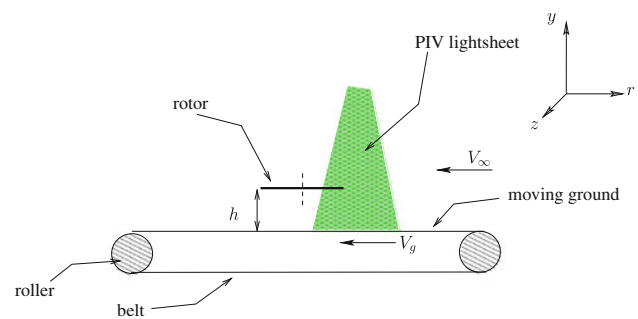

Fig. 4 Schematic diagram of rotor model, moving ground (rolling road), PIV light sheet and sense of moving ground and wind tunnel speeds V_g and V_∞. The sense of the coordinate system is shown, but its origin is at the *centre* of the rotor disk

provided information on the torque provided by the motor; torque limitations meant that the rotor was run at a speed of $n = 16$ revolutions/s. The rotor blades were untwisted, untapered and mildly cambered with a chord length of $c = 5.5$ cm and thickness-to-chord ratio 12%. The rotor assembly was mounted on a sturdy plate, which in turn was fixed to a sting support through a system of four load cells, each of which provided vertical force information only but could still transmit horizontal force. Blade cyclic angles could be set such that the vertical force centroid was acting through a desired point. A 16-bit data acquisition card connected to a PC provided real-time data of the load cell forces, thus allowing rotor thrust to be determined. The entire rotor assembly was mounted at the centre of the working section on the end of a long sting that allowed its height h above the ground to be varied. For these tests, the rotor shaft was set with no tilt and the rotor disk was in the horizontal plane.

The wind tunnel itself was capable of a speed $V_\infty = 70$ ms^{-1} but for the purposes of the current tests, the speed was no higher than around 10 ms^{-1}. The bottom surface of the wind tunnel working section was fitted with a 1.9 m wide, 3.9 m long moving ground consisting of a belt, powered by large, circular rollers, moving over a flat, steel platen. While the moving ground could be set at an arbitrary speed relative to the wind tunnel speed, the tests were conducted with the moving ground speed set to either ground stationary relative to the rotor, $V_g = 0$, or with zero speed relative to the wind tunnel flow, $V_g = V_\infty$. The former condition is equivalent to the rotor stationary over the ground with the air moving past the rotor/ ground system (hover in a cross-wind), while the latter condition is representative of forward flight at speed V_∞ over the ground into a still atmosphere. The moving ground system was equipped with a suction device to remove the boundary layer, but this was designed for use at much higher wind tunnel speed where the boundary layer would be thinner and was not used in these experiments.

A commercial system (LaVision) was used for the PIV. This was based on a dual-cavity, Nd:YAG laser, output wavelength 532 nm, capable of delivering 0.5 J/pulse (8 ns duration), and two 14-bit, 4,008 × 2,762 pixel (11 Mpixel) digital video cameras. Each camera was fitted with 100 or 50 mm lenses ($f_\# = 2.8$) mounted on Scheimpflug tilting lens mounts for sharp focus across the field of view when viewing off axis, and the system was operated using one camera in two-component mode for the (u, v) velocity field in the (r, y) plane, or with both cameras in stereoscopic, three-component mode for the (u, v, w) velocity field in the (r, y) plane. z-component vorticity ω was calculated from the (u, v) velocity. The laser was expanded into a 2-mm-thick laser sheet, located in the vertical plane, parallel with the wind tunnel longitudinal axis and coincident with the mid-plane of the rotor disk. Due to the size of the rotor and its wake, the field of view was typically around 1 m (one rotor diameter) wide, and the PIV time delay employed was 300 μs for this field of view. A Laskin nozzle seeder was used with olive oil as the substrate, and this generated a fine oil mist with nominal particle diameter 1 μm; the particle relative density and size are known to be good for PIV in air, and the only area where particle acceleration effects were apparent was in the very young trailed vortices immediately below the rotor disk. LaVision Davis version 7.2 software was used for data reduction, and an iterative scheme was used with a final PIV window size of 32 × 32 pixels with 50% overlap, equivalent to one velocity measurement per 4 mm^2 for a 1-m-wide field of view. Up to 120 cases were sampled per test, sufficient for an estimation of the mean-flow velocity and other statistics. To characterise the trailed vortex system just below the rotor disk in more detail, two-component PIV was carried out using a 200 mm, $f_\# = 4$ focal length lens; this provides a spatial resolution of one velocity measurement per 1.8 mm^2, useful for determining trailed vortex diameter and circulation Γ close to the rotor disk (see Sect. 3.1). Where possible, the PIV sampling was performed independent of rotor phase. However, in some cases, the presence of the rotor in the field of view would cause excessive laser shadow or glare (this latter condition can damage the camera CCD chip). In these cases, it was necessary to phase the PIV sampling with rotor azimuth at 45°. Post-processing of PIV data was performed using bespoke codes written in MATLAB.

The sense of rotor trim needs to be defined. The advance ratio alters the shape of the wake and the rotor inflow, and hence the rotor trim condition. It was therefore essential that the rotor could be operated as close to the same trim condition as possible as the flow conditions changed, and this is why the rotor system was designed with variable cyclic angles. A wind tunnel 'trim' here is defined as when the vertical force centroid is acting through the centre of the rotor disk. The vertical force centroid position was determined from the system of four load cells. The side forces were not known, so the condition with the vertical force centroid acting through the centre of the rotor disk is not the same as zero rolling and pitching moment, but the condition will be referred to as 'trimmed' for convenience. In the 'untrimmed' condition, the cyclic angles were set to zero.

2.1 Validity of experimental approach and accuracy of results

Rotor testing in wind tunnels is challenging. The objective of these experiments was to investigate the fluid dynamics

of the rotor wake IGE, and not to determine performance data. Barlow et al. (1999) suggest maximum model-span-to-tunnel-width-ratios; the current model rotor diameter is within these limits and is comparable to other experiments cited. Leishman (2006) presents a brief discussion of wind tunnel effects, and it is widely acknowledged that testing is especially difficult at low advance ratios. As small a diameter rotor or as large a wind tunnel as possible is ideal. Resolution of the tip vortices and their effect on the flow at the ground was important, so for the purpose of investigating the fluid dynamics a larger rotor size was important. Experience had been gained using a 0.15-m-diameter rotor in a smaller tunnel (1.05 m wide), (Nathan and Green 2009), so a simple, 0.3-m-diameter rotor was built for the larger tunnel used for these tests, with the aim of comparing wake geometry with the larger rotor system. Further discussion will be presented in Sect. 4. Flow Reynolds numbers are also presented and discussed in Sect. 3.

Calibration and measurement indicated that the rotor cyclic pitch angles could be measured to an accuracy of 0.05° using the linear potentiometers, and the load cell system for thrust measurement was capable of resolving a force of 0.05 N, or 0.2% of the thrust level. Accuracy with the rotor running was compromised due to vibration, but the rotor was run far from a resonant frequency. A realistic assessment of rotor thrust accuracy with the rotor running was 1%, and with care the rotor thrust centroid could be set to within 5 mm of the rotor axis, equivalent to a cyclic angle setting accuracy of 0.1°.

Calibration for the PIV was undertaken with great care. The calibration pattern consisted of a large grid of circular dots with fiducial markers for camera alignment. The calibration grid was aligned with the laser sheet to within the laser sheet thickness over the width of the field of view, and careful adjustment of the Scheimpflug mounts was made to ensure sharp focus across the field of view. Multiple images of the calibration grid at small, arbitrary pitch and yaw angles were taken according to the PIV system instruction manual. Correlation coefficients calculated by the calibration scheme were satisfactory and within the system manufacturer's guidelines. The choice of PIV time delay was to avoid bad correlation in the vicinity of the vortex cores close to the rotor disk where the out-of-plane velocities were large and in-plane velocities were highest, and the time delay used at large field of view gave a notional 5 pixel displacement for the scaling velocity V_h. Fresh vortex cores close to the rotor were relatively devoid of seeding, but there was no noticeable effect of this on the PIV results. Otherwise, the most serious issues for the PIV were difficult optical access in the wind tunnel and glare off the ground. Glare was reduced to tolerable levels by placing the cameras as close to the ground as possible to reduce incident angles, but it was found that useful

measurement closer than 5 mm to the ground was not reliable as PIV data there were affected by the ground glare. There was also the issue of the out-of-focus background of the ground biasing velocity measurements higher up in the velocity field, but the low incident angle of the cameras helped to prevent this. In view of these difficulties, the cameras were adjusted so that they only recorded images above around 5 mm from the ground surface. The performance of the stereo PIV was benchmarked by taking measurements of a uniform flow, for which there were no significant (u, v, w) velocity gradients across the field of view. This at least validated the stereo PIV procedure. Stereo PIV (u, v) data were compared with two-component PIV data for the same region of the rotor flow, which in turn were compared with the results of analysis of PIV by an independent method; there were no consistent discrepancies and differences were negligible. The peak-locking effect in the PIV velocity maps was calculated by DaVis 7.2 to have an average value of 0.0651, observed to be well within the published acceptable range of <0.1 (DaVis 2007). Absolute accuracy of the PIV was better than 2%, which is adequate for a quantitative analysis of the flow. Velocity derivatives were calculated using the least squares approach (see Raffel et al. 1998), and bespoke codes were written for this.

3 Results

The rotor model was tested in the wind tunnel for normalised advance ratio in the range $0.3 < \mu^* < 1.0$ and ground height $\frac{h}{D}$ 0.5 and 1.0, with the rolling road set to the stationary condition $V_g = 0$ (hover in cross-flow), or, for a representative simulation of forward flight close to the ground, with the ground moving at the same speed as the wind tunnel, $\frac{V_g}{V_\infty} = 1$. Most of the results presented in this paper are for the blade collective angle 8.8°, but some results for 12.8° are also shown. Non-dimensional data are presented in this paper. The rotor radius $R = 0.5$ m is used as an appropriate length scale, and the hover-induced velocity $V_h = V_{tip}\sqrt{C_T/2}$ is used as the appropriate velocity scale for scaling flow velocity (thus vorticity is scaled with $\frac{V_h}{R}$). The (r, y, z) coordinate system is shown in Fig. 4, but note that the origin of the coordinate system is at the centre of the rotor disk. The present section briefly describes the rotor and trailed vortex characteristics and the effect of the moving ground on the flow before considering the more detailed fluid dynamics of the ground effect wake. PIV data are presented in terms of mean and instantaneous flow 2D pathlines, and mean and instantaneous velocity and vorticity. The mean and instantaneous flow pathlines were produced from (u, v) velocity data; virtual particles

Fig. 5 Instantaneous flow pathlines, (**a**), and non-dimensional vorticity (**b**), in the ground effect wake at $\mu^* = 0.52$ for the trimmed rotor at height $h/D = 0.5$ *above* the ground, ground moving at $\frac{V_g}{V_\infty} = 1$. Rotor collective angle 12.8°. The rotor disk is shown by the *horizontal, dashed line*, and the direction of the wind tunnel flow from *right* to *left* is shown on the vorticity *plot*
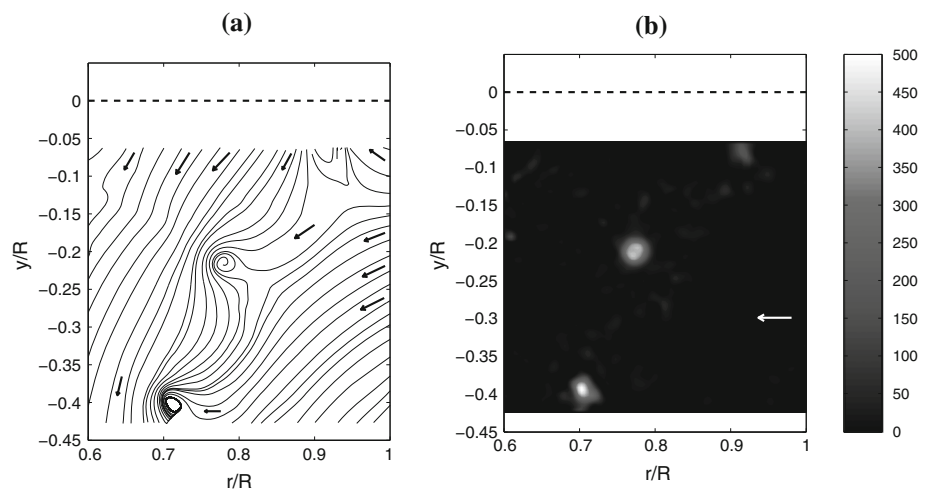

Table 1 Rotor collective, thrust and trailed vortex characteristics

Collective angle (°)	C_T	V_h (ms^{-1})	Re_Γ	$\frac{\Gamma}{cV_h}$
8.8	0.0100	3.55	60,000	4.7
12.8	0.0147	4.35	75,000	4.8

were released into the flow field at seed points and allowed to convect through the flow according to the (u, v) data as if it were a steady flow. The pathline plots are therefore artificial, but they serve as a useful guide to the flow field. Other parameters are extracted from the velocity data as required.

### 3.1 Trailing vortex strength, rotor characteristics and flow Reynolds numbers

Trailed vortex characteristics were determined using two-component PIV (u, v) data with the camera fitted with the 200-mm focal length lens. Figure 5 shows a typical instantaneous result for a collective angle of 12.8° with the rotor at $\frac{h}{D} = 0.5$ and a normalised advance ratio of $\mu^* = 0.52$. Instantaneous streamlines (pathlines) formed from the velocity field are shown together with non-dimensional vorticity. The trailed vorticity is positive, and peak non-dimensional vorticity values are around 500. Complete vortices at $y/R = -0.2$ below the rotor were interrogated, corresponding to a vortex age (in terms of rotor rotation) of 135°. They were compact and well formed. The vortex diameter was defined in terms of a low-level vorticity threshold with a mean diameter measurement, and also by investigation of the vortex radial velocity distribution. The vortex diameter was 1.7 cm or 0.034R, therefore the vortex core radius is $r_c = 0.15c$. The spatial resolution of the PIV system with the 200-mm focal length lens is $L_m = 1.8$ mm, so $L_m/r_c = 0.21$, which is just outside threshold value of

$L_m/r_c \leq 0.2$ suggested by van der Wall and Richard (2006). The purpose of the current work is not to investigate the characteristics of the trailed vortices themselves, but the resolution of the PIV used in this mode is just sufficient to provide the vortex radius value at this wake age and provides useful information for characterising the experiment. Circulation Γ is presented in terms of circulation Reynolds number $Re_\Gamma = \frac{\Gamma}{\nu}$, where ν is the kinematic viscosity, and non-dimensional circulation $\frac{\Gamma}{cV_h}$. Important rotor characteristics are shown in Table 1. A representative blade Reynolds number Re_c is based on blade chord c and V_{tip} and $Re_c = 182,000$. With reference to results shown in Table 1, adjustments to the blade collective angle showed proportional increases in rotor thrust, trailed circulation strength and Re_Γ, but no significant change to the value of $\frac{\Gamma}{cV_h}$, and this indicates predominantly attached flow behaviour over the blades. The compact vortex size and the value of Re_Γ imply that the flow is inertia dominated (Chen et al. 1999).

3.2 Effect of moving ground on ground effect wake

Figure 6 shows results from the PIV measurements of the ground effect wake at ground height $\frac{h}{D} = 0.5$ and normalised advance ratio $\mu^* = 0.76$. The rotor is trimmed, and the figures show mean-flow pathlines and non-dimensional vorticity for ground stationary and ground moving tests. The effect of the moving ground on the flow is remarkable. The wind tunnel flow direction is shown, the position of the rotor disk is indicated by the dashed, horizontal line and the ground is at $y/R = -1$. Vorticity contour levels have been selected to highlight the flow in the vorticity regions close to the ground, and non-dimensional vorticity contours are plotted in the range $-21 < \frac{\omega}{V_h/R} < 21$. Contour lines are also indicated to help highlight vorticity values; the minimum vorticity magnitude shown is 1, the next magnitude plotted

Fig. 6 Mean-flow pathlines
(**a** and **b**), and non-dimensional
vorticity (**c** and **d**), in the ground
effect wake at $\mu^* = 0.76$ for the
trimmed rotor at height $h/D = 0.5$ *above* the ground.
a and **c** are for the ground
stationary (mean-flow pathlines
and vorticity, respectively),
(**b** and **d**) are for the moving
ground (mean-flow pathlines
and vorticity, respectively). The
rotor disk is shown by the
horizontal, *dashed line*, and the
direction of the wind tunnel
flow from *right* to *left* is shown
on the vorticity *plots*. Vorticity
contour levels have been
selected to show detail in the
fluid close to the ground.
a Pathlines, $V_g/V_\infty = 0$,
b pathlines, $V_g/V_\infty = 1$,
c vorticity, $V_g/V_\infty = 0$,
d vorticity, $V_g/V_\infty = 1$
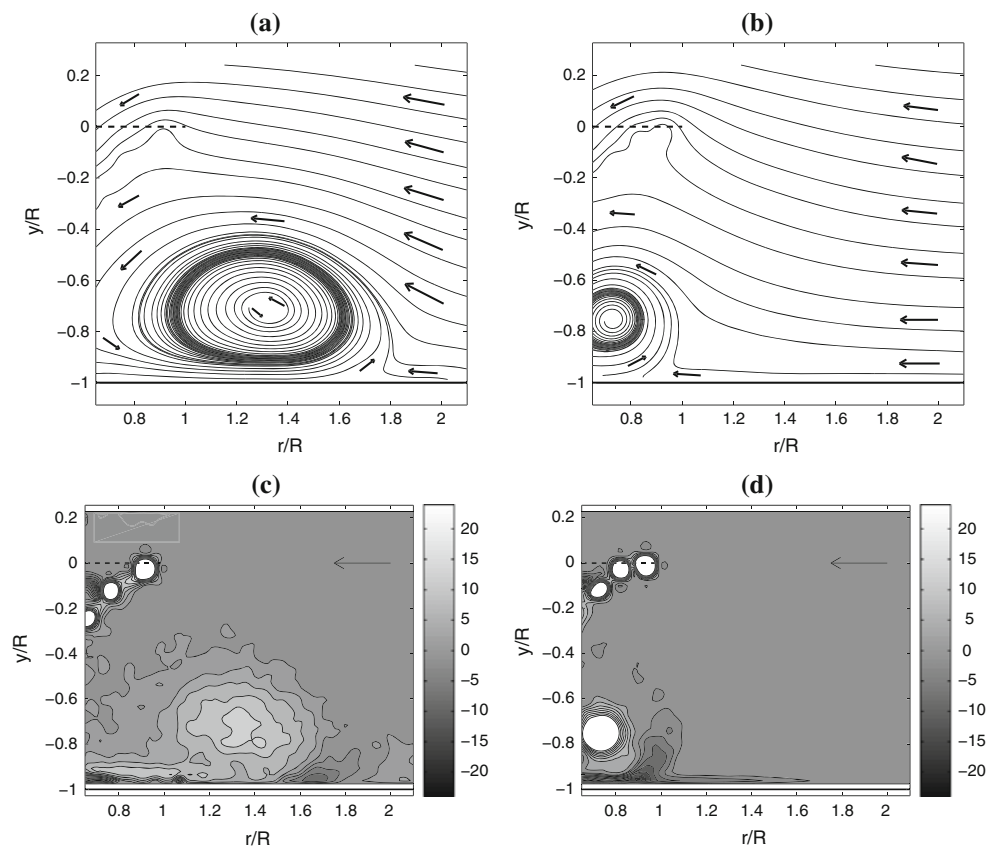
is 3 and the contour increment is then ± 3. The contour plots are saturated in areas of high positive vorticity; in the area around the lower left of frame (d), the peak positive vorticity is 41, and the distinct spots of positive vorticity around the area $(r, y)/R = (0.6, -0.1)$ just below the rotor disk have maximum vorticity levels around 100. These are the trailed vortices, and they remain distinct in spite of the averaging process because the PIV system has been phased locked with azimuth (at $\psi = 45°$). Peak vorticity levels observed in instantaneous results are significantly higher. Patches of negative vorticity appear in the flow close to the ground, but there is also a small patch at the extreme left of the image just below the rotor; this is due to an artefact caused by poor illumination at the edge of the PIV light sheet.

The salient feature in all the plots is the recirculation zone due to the ground effect, and this is shown by the clear pathline recirculation around $y/R = -0.7$. Flow approaching the rotor lower down in the field of view and upstream of the recirculation zone passes up and around the recirculation zone, while higher up in the field of view fluid is deflected upwards and passes down through the rotor disk. The mean-flow pathline topologies also show a separation point on the ground ahead of the recirculation zone, around $r/R = 1.7$ in the stationary ground case, and $r/R = 0.9$ in the moving ground case. Vorticity plotted in frames (c) and (d) shows the vortices trailed from the tip as the

spots of high, positive vorticity strung down and to the left from the leading edge of the disk at $(r, y)/R = (1, 0)$. In frame (c) for the stationary ground, the trailed vortices follow a trajectory down to the ground, and they then turn upstream. A thin ribbon of strong, positive vorticity is seen close to the ground, and the positive mean-flow vorticity accumulates in the large recirculation zone suggested by the mean-flow pathlines. There is a small area of negative vorticity close to the ground to the right of the region of positive mean-flow vorticity at around $\frac{r}{R} = 1.7$, and this is coincident with the topological separation point, and this suggests the presence of a much smaller, secondary vortex system. Frame (d) for the moving ground case shows that the vorticity magnitude in the mean-flow recirculation zone is far higher than for the non-moving ground, but the positive vorticity is confined to a much smaller area. Compared with the stationary ground, there is now an area of strong, negative vorticity between the recirculation zone and the ground, and this curls up into the flow from around the location of the topological separation point in the mean flow at $r/R = 0.9$ to form an arc of weak negative vorticity passing almost completely around the recirculation zone.

The negative vorticity close to the ground in Fig. 6 frame (d) extends in a thin, narrow band ahead of the separation point to around $r/R = 1.6$. The mean-flow pathline pattern in frame (b) shows deceleration of the flow

approaching the recirculation zone in the region below $y/R = -0.8$. This is owing to the wind tunnel flow from right to left being progressively opposed by the induced velocity effect from left to right due to the recirculation system (itself strengthened significantly IGE by the notional 'image' of the vortex system below the ground). The wake-induced velocity effect becomes stronger closer to the recirculation system and will be at its maximum along the plane of the ground. At the ground, the flow speed must be equal to the ground speed, and this frictional effect sets up a boundary layer ahead of the wake, thus accounting for the forward protruding tongue of negative vorticity along the ground. u-component velocity profiles ahead of the topological separation point are presented in Fig. 7 for the moving ground case shown in Fig. 6, $V_g/V_\infty = 1$. The maximum magnitude u velocity is $u/V_\infty = -0.45$, showing the extent to which the induced velocity effect opposes the wind tunnel flow. At the ground, where PIV data were not available, $y/R = -1$ and $u/V_\infty = -1$. A similar upstream-induced velocity and boundary layer effect is present in the ground stationary case except negative vorticity is not observed since at the ground $u/V_\infty = 0$.

The above changes to the physical extent of the ground effect wake can be summarised in terms of the forward topological separation point of the mean flow ahead of the recirculation zone, and the enstrophy dispersion radius E_N in a domain S of the flow field defined by

$$r_{E_N}^2 = \frac{1}{E_N} \int_S |\mathbf{x} - \mathbf{x_{E_N}}|^2 \omega(\mathbf{x})^2 \mathrm{d}S \qquad (1)$$

where $E_N = \int_S \omega^2 \mathrm{d}S$ is the integrated enstrophy in the domain S, $\mathbf{x}$ is a vector position in the flow field and $\mathbf{x_{E_N}}$ is
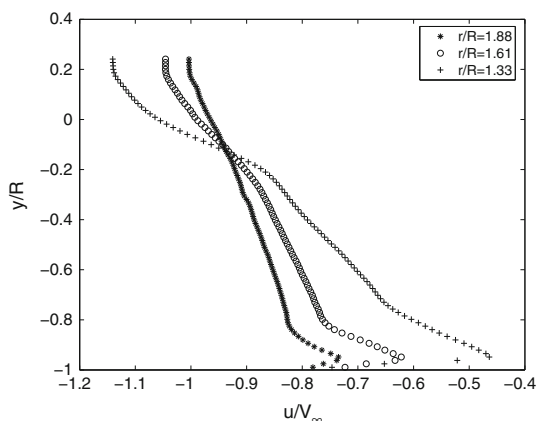

Fig. 7 u-component velocity profiles *plotted* as a function of vertical ordinate y/R at three longitudinal distances ahead of the rotor for $\mu^* = 0.76$, rotor height $h/D = 0.5$, ground moving $V_g/V_\infty = 1$. Recirculation system induced u velocity is in the positive direction, wind tunnel and ground velocity are in the negative direction

the vector position of the enstrophy centroid. Enstrophy is a preferable property to circulation for the current purposes as the flow contains mixed areas of positive and negative vorticity. The domain S is defined as the extent of the recirculation zone. The forward separation point of the flow is defined as a topological separation point and is found from the (u, v) data closest to the ground where the u-component changes sign. Enstrophy dispersion radius and separation point data for a range of normalised advance ratio for trimmed and untrimmed cases with the ground condition at stationary, $\frac{V_g}{V_\infty} = 0$, and moving, $\frac{V_g}{V_\infty} = 1$, are shown in Fig. 8. The data shown are the mean values of the individual cases. For a given normalised advance ratio, it can be seen that the effect of the moving ground is to push the separation point back closer to the rotor by around $0.5R$. The reduction in the enstrophy dispersion radius r_{E_N} is greatest at the higher normalised advanced ratio, where the recirculation zone is almost half as small compared with the stationary ground case. These measurements reflect the description of Fig. 6 above at $\mu^* = 0.76$. Changing the trim condition has only a weak effect, however, with the adjustment from untrimmed to the wind tunnel trim moving the separation point towards the rotor by approximately $0.1R$ and reducing r_{E_N} by only a small amount.

3.3 Influence of normalised advance ratio

Although the effect of forward flight speed on the position and size of the ground effect wake is well known, and the description in Sect. 3.2 above reflects this, additional investigation was conducted to reveal phenomena in the ground effect wake. Figure 9 shows mean-flow pathline and vorticity plots at advance ratio $\mu^* = 0.40$ and 0.66, for the rotor trimmed and ground moving $\frac{V_g}{V_\infty} = 1$ condition for a rotor height $\frac{h}{D} = 0.5$. The reader is also referred to frames (b) and (d) of Fig. 6 for $\mu^* = 0.76$, and the contour lines are at the same level. As suggested in the plots of r_{E_N} and separation point, the figures show that the wake shrinks in size and forms closer to the rotor as μ^* increases. At $\mu^* = 0.40$, the large recirculation zone is quite far ahead of the rotor, and it is connected to the trailing vortex system below the rotor by a thin ribbon of positive vorticity close to the ground. As advance ratio increases, vorticity levels within the recirculation zone become much higher, but the structure within the zone at moderate advance ratio, frame (d) at $\mu^* = 0.66$, shows highest positive vorticity levels in a ring around the centre of the recirculation zone. Figure 6 frame (d) for higher advance ratio has maximum positive vorticity in the centre of the much smaller recirculation zone. In each case, a thin layer of negative vorticity forms below the mean-flow recirculation, which then

Fig. 8 Effect of moving ground and trim condition on **a** mean enstrophy dispersion radius and **b** mean topological separation point, over a range of normalised advance ratio
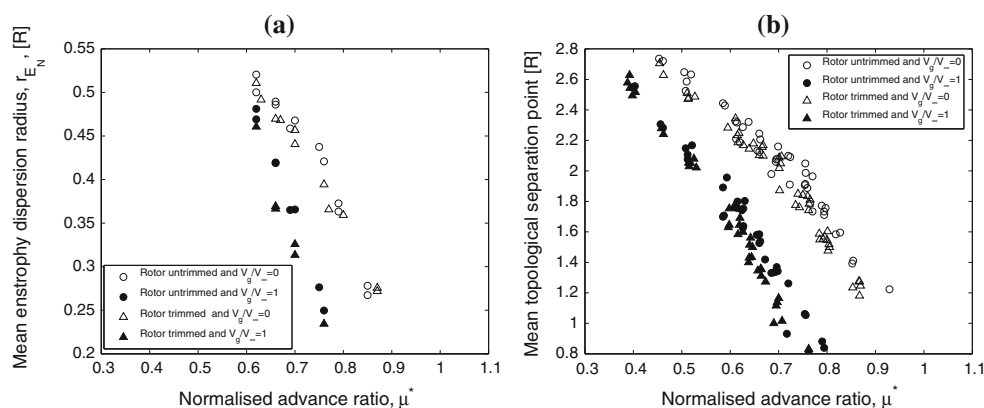
curls up into the flow from the separation point to form a weak band around the edge of the positive vorticity recirculation zone.

3.4 Cross-flow behaviour

Stereo PIV was used to examine the significance of the cross-flow velocity component w, and Fig. 10 frame (a) shows a contour plot of w velocity at $\mu^* = 0.67$ in the mid-plane of the flow. Difficulties with optical access in the wind tunnel led to the presence of velocity artefacts at the extreme lower corners of the images, and these need to be considered in the interpretation of the results. Owing to the direction of rotation of the rotor, the wake velocity deficit is a negative velocity. At very low advance ratio, the cross-flow velocities in the mid-plane of the recirculation zone are negligible. In the figure, the velocity deficit in the trailed vortices can be seen as the spots of negative w close to the left-hand edge just below the rotor disk. The structure of the cross-flow in the recirculation zone shows some interesting features, and this is why the mean-flow pathlines, frame (b), have also been plotted. There is strong negative w around the separation point, but the recirculation zone itself is marked by weak positive and negative w; the lowest negative w is at $(r, y) = (1, -0.75)R$, and the highest positive w is at $(r, y) = (1.3, -0.56)R$. For brevity, the vorticity for this test case is not shown, but the positive vorticity centroid is around $(r, y) = (1, -0.67)R$, and the reader is referred to Fig. 9 frame (d) for the vorticity at a similar advance ratio. The area of negative w is coincident with the positive vorticity region of the recirculation zone, but the positive w flow lies to the upper right, and only just overlaps the positive vorticity fluid. The negative w is associated with the trailed vortex wake velocity deficit, while the positive w is due to the external fluid passing around the recirculation zone, which extends around the rotor as a horseshoe vortex.

4 Discussion

The results described above illustrate the importance of the correct representation of the ground to rotor relative velocity in an experimental simulation of forward flight of a rotor IGE in a wind tunnel. Detailed flow visualisation tests using PIV, however, suggest that the effect of the rotor trim condition on the flow itself is not so significant. The rotor size used for the experiments was chosen on the basis of experience elsewhere, but the large size of the ground effect wake is acknowledged. To assess whether wind tunnel constraint was significant enough to affect the fluid dynamics, tests with a smaller rotor of 0.3 m diameter (not trimmed) were performed. The ratio of rotor diameter to tunnel width for this rotor was 0.11 compared with 0.37 for the larger rotor system. Comparison of the results showed broadly similar features at all but the very lowest normalised advance ratio, and the effect was less significant for the ground moving case, $V_g/V_\infty = 1$, where the wake was smaller. Above $\mu^* = 0.5$, the ground separation point was slightly closer to the rotor for the small diameter case. At lower advance ratio, the separation point for the large rotor was closer to the rotor, and the difference in separation point positions only became significant below $\mu^* = 0.4$ where the flow more closely resembles hover anyway. Results of tests with the smaller rotor suggest that the fluid dynamics do not appear to be significantly affected by wind tunnel constraint at the advance ratios of interest.

4.1 Changes of flow regime

Curtiss et al. (1984) describe flow regimes based on their flow visualisation measurements, and their recirculation regime was characterised by wake fluid passing through the rotor disk. Wake fluid contains vorticity, so similar observations ought to be possible using the current PIV data. The flow in a rectangular zone (named Υ for
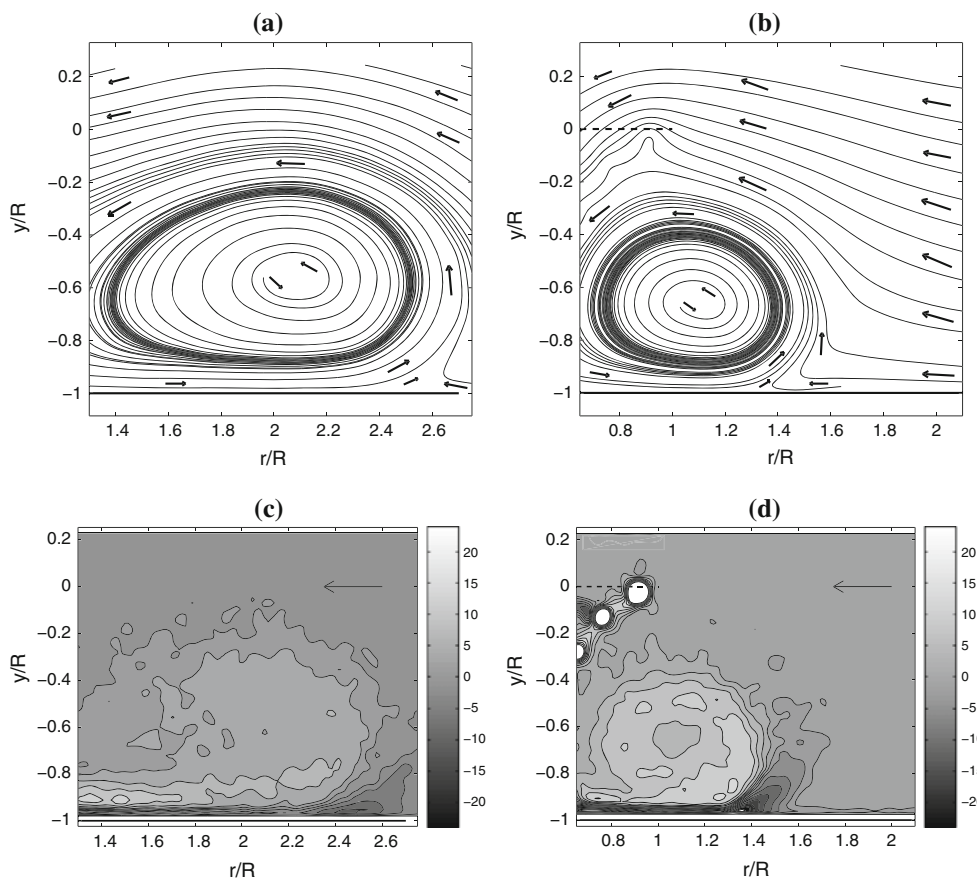
Fig. 9 Mean-flow pathlines and vorticity (non-dimensional) for two advance ratios, (**a** and **c**) at $\mu^* = 0.40$ and (**b** and **d**) at $\mu^* = 0.66$. Trimmed rotor, ground moving $\frac{V_g}{V_\infty} = 1$, rotor at height $h/D = 0.5$ *above* the ground. The rotor disk on (**b** and **d**) is shown by the *horizontal*, *dashed line*, and the direction of the wind tunnel flow from *right* to *left* is shown on the vorticity *plots*. The reader is referred to Fig. 6, frames (b) and (d), for the test at $\mu^* = 0.76$, which complements this sequence. **a** Pathlines, $\mu^* = 0.40$, **b** pathlines, $\mu^* = 0.66$, **c** vorticity, $\mu^* = 0.40$, **d** vorticity, $\mu^* = 0.66$
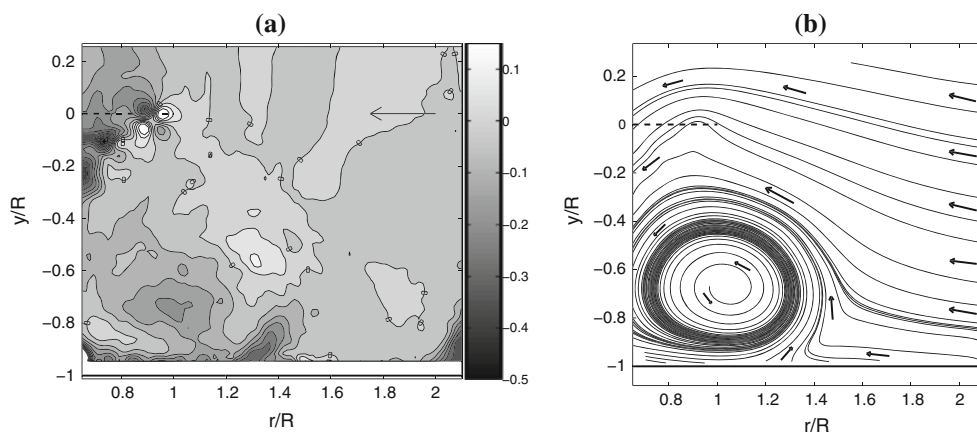

Fig. 10 Mean cross-flow (*w*-component velocity) plot, (**a**), scaled with V_h and mean-flow pathlines, (**b**), for $\mu^* = 0.67$ with the rotor trimmed and the ground moving ($V_g/V_\infty = 1$). The rotor direction of movement corresponds to negative *w*. The rotor is at a ground distance of 0.5D, and the rotor disk is shown by the *horizontal*, *dashed line*. The features in the *bottom left* and *right* corners of **a** are artefacts due to difficulties with optical access for the stereo PIV. The zero *w* contour in **a** is *labelled* for clarity. **a** *w* Component, **b** pathlines
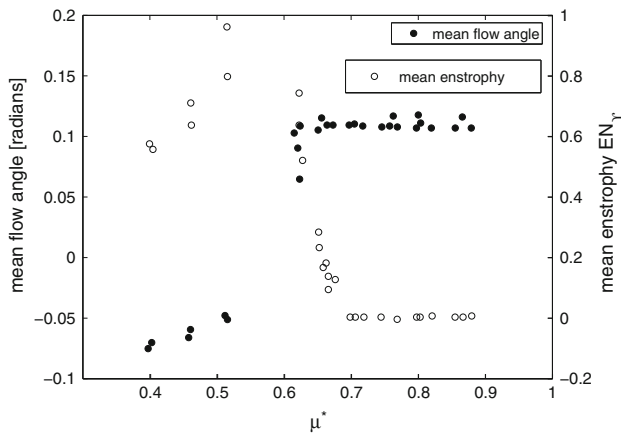
Fig. 11 Mean-flow angle and mean enstrophy EN_Υ in the rectangular zone Υ defined by coordinates $(r, y)/R = (1.2, 0)–(1.6, 0.2)$ as a function of μ^*. Data for rotor trimmed and the ground moving $(V_g/V_\infty = 1)$

convenience) defined by coordinates $(r, y)/R = (1.2, 0)–(1.6, 0.2)$ just ahead of the disk leading edge and above the rotor disk plane was investigated. Due to the presence of positive and negative vorticity, enstrophy ω^2 was used to label wake fluid. Mean in-plane flow angle and mean-flow enstrophy EN_Υ in zone Υ are shown in Fig. 11 for a range of μ^*. At low advance ratio, the enstrophy content and flow direction in the area remain high and downward, respectively, as μ^* increases, but for higher μ^*, the mean-flow direction changes to upflow and the mean enstrophy content in this zone drops to almost zero. It should be noted that the change of flow angle is seen clearly on the pathline plots on Fig. 9 frames (a) and (b) in the $r/R = 1.4$ region at positive y. Therefore, at low advance ratio, wake fluid is observed high up in the flow, and this fluid tends to pass back down through the rotor disk, compatible with the observations due to (Curtiss et al. 1984). It is useful to consider a definition of recirculation regime based on vorticity.

4.2 Details of unsteady wake flow behaviour

The above descriptions of mean-flow behaviour hide how the flow in the ground effect wake can change with time. The PIV was not time resolved, but instantaneous snapshots reveal the extent of the temporal changes. As in Sect. 4.1, it is useful to pay particular attention to how high up in the field of view vorticity appears, and the definition of the zone Υ [the rectangle $(r, y)/R = (1.2, 0)–(1.6, 0.2)$] is used to illustrate differences in the flow-field snapshots. Figure 12 shows instantaneous vorticity plots for the case corresponding to the mean flow shown in Fig. 9 at $\mu^* = 0.66$, rotor trimmed, ground moving at $\frac{V_g}{V_\infty} = 1$, rotor at 0.5D above the ground. At this μ^*, the mean enstrophy in

zone Υ is falling as advance ratio rises. Frame (a) in the figure shows positive and negative vorticity in Υ, while frame (b) shows no vorticity. In both cases, the flow velocity vectors show the flow in a direction similar to the mean-flow pathlines depicted in Fig. 9 frame (b). At lower advance ratios, where the recirculation zone is larger, proportionally more of the samples have significant vorticity in zone Υ, while at higher μ^* progressively fewer samples bearing vorticity in Υ are seen. It is convenient to define a mean enstrophy content threshold $EN_T = 0.05$ in zone Υ, and plot how the proportion of PIV samples with mean enstrophy $EN_\Upsilon > EN_T$ changes with μ^*, and this is shown in Fig. 13 for the ground moving case with stationary ground data for comparison. At very low μ^*, the majority of samples (>80%) show $EN_\Upsilon > EN_T$, but this proportion decreases rapidly to zero in the range $0.6 < \mu^* < 0.7$; at high enough μ^*, wake fluid is not observed at all in zone Υ. The ground stationary case vorticity bearing fluid in the same zone at higher μ^*, and a gentler rate of reduction from lower μ^* as advance ratio rises; the wake in the ground stationary case is more diffuse at the same μ^*. If the recirculation regime of Curtiss et al. (1984) is defined in terms of wake fluid, then the observations of the instantaneous vorticity here suggest a transition regime in which the mean flow rapidly changes from recirculation regime to ground vortex regime, but individual snapshots of the flow could be in either state.

4.3 Ground effect flow regimes

The above discussions describe gross changes in flow behaviour, in addition to more subtle characteristics. Ground effect flow regimes defined in terms of vorticity in region Υ are proposed. In the recirculation regime, there is frequent reingestion of wake fluid (indicated by enstrophy) through the rotor disk, and in the ground vortex regime, this never happens. Table 2 shows a comparison of the ground effect flow regimes observed from the current PIV data with those described by Curtiss et al. (1984). These changes in vorticity reingestion are accompanied by changes in mean-flow direction in the same area from downflow to upflow. Table 2 shows the flow regimes determined from the current PIV tests with the ground moving and stationary, and it is seen that for the ground stationary, $V_g/V_\infty = 0$, the flow regimes occur at higher μ^*. It should be noted that Boer et al. (2001) presented upper and lower limits of a ground vortex regime in their analysis of PIV and laser light sheet data. They did not use a rolling road, and the number of data points is sparse and their definition of ground vortex analysis appears to be based on the position of a vortex in the field of view.
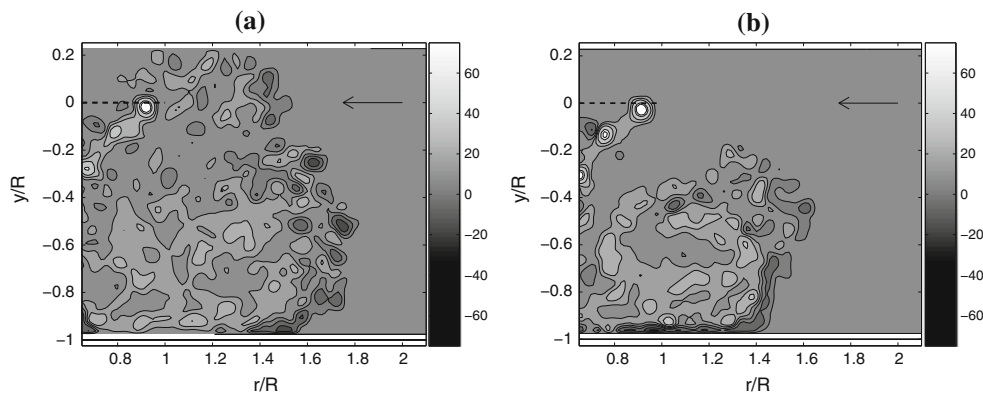
Fig. 12 Instantaneous vorticity (non-dimensional) for $\mu^* = 0.66$ with the rotor trimmed and the ground moving ($V_g/V_\infty = 1$). The mean-flow vorticity is shown in Fig. 9 frame (d). **a** has high enstrophy in the zone Υ defined by $(r, y)/R = (1.2, 0)$–$(1.6, 0.2)$, while the

same region of flow in **b** at a different time is vorticity free. In both cases, the minimum vorticity magnitude plotted is 5, and the vorticity contour levels are at increments of ± 15. **a** Case 76, **b** case 62
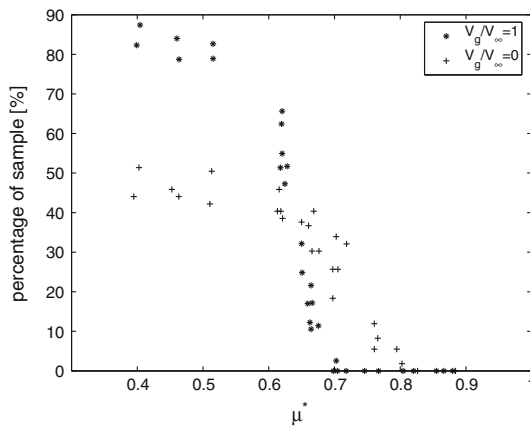

Fig. 13 Proportion of samples with mean enstrophy $EN_\Upsilon > EN_T$ in the rectangular zone Υ as a function of μ^*, ground stationary and ground moving cases shown for comparison

4.4 Rotor trim behaviour

It is well known that there are distinctive changes in helicopter trim behaviour IGE, and the current results allow these trim changes to be attributed to ground effect wake structure. Longitudinal and lateral cyclic angles for achieving wind tunnel trim are indicated in Fig. 14. Longitudinal cyclic data are only shown for the ground moving case, but lateral cyclic data are shown for both ground

moving and ground stationary. The scatter on the data is owing to vibration causing uncertainty in setting the trim condition. For the ground moving case, both trim inputs increase at around the same rate as μ^* increases from 0.4, but the required lateral cyclic angle begins to increase more rapidly above around $\mu^* = 0.64$ [it is this particular aspect of helicopter trim IGE forward flight that is well known (see for example Prouty 1985)]. The solid line is a fit to the lower advance ratio lateral cyclic data, and the dashed line is the extrapolation of this to higher μ^*, which helps to emphasise the change of trim behaviour between low and high μ^* ranges. The scatter in the trim data makes a precise demarcation point difficult to define, but given the description of the unsteady flow behaviour described above, a well-defined point is unlikely. The stationary ground data show a similar rate of change of lateral cyclic trim input with increasing μ^*, but no distinct change of behaviour around $\mu^* = 0.64$, but there appears to be an increase in gradient around $\mu^* = 0.85$.

Separation point position and wake size in Fig. 8 show no such change in behaviour with increasing μ^* for the moving ground case. Instead the change to trim behaviour observed in the moving ground case can be attributed to the inflow angle in the region of the leading edge of the disk, coincident with wake fluid disappearing from the area above the rotor disk, and this is due to the gradual wake shrinkage and its

Table 2 Comparison of the ground effect flow regimes identified from the PIV analysis with results published by Curtiss et al. (1984)

	Curtiss data μ^*	Current PIV data $V_g/V_\infty = 1$ μ^*	Current PIV data $V_g/V_\infty = 0$ μ^*
Ground distance	0.45D	0.5D	0.5D
Recirculation regime	$0.4 < \mu^* < 0.64$	$0.4 < \mu^* < 0.66$	$0.6 < \mu^* < 0.9$
Ground vortex regime	$0.64 < \mu^* < 0.83$	$0.66 < \mu^* < 0.8$	$0.9 < \mu^* < 1.0$

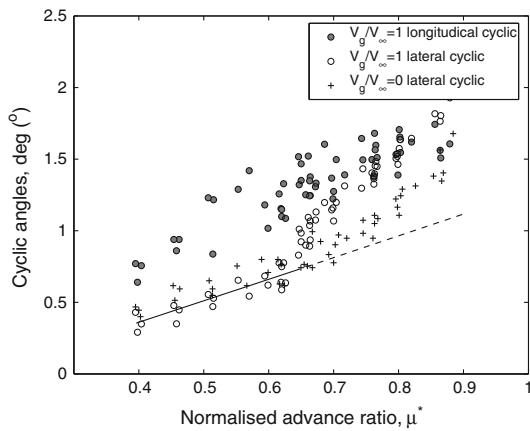Results from the current tests are with the rotor trimmed

Fig. 14 Longitudinal and lateral cyclic trim inputs to achieve wind tunnel trim for rotor at ground height $h = 0.5\ D$ with 8.8° collective with the ground moving ($V_g/V_\infty = 1$). The *solid line* is a fit to lateral cyclic data at low μ^*, and the *dashed line* is an extrapolation of this to higher μ^*. Lateral cyclic data for the non-moving ground are also shown for comparison

downstream movement with increasing μ^*. With the ground moving $V_g/V_\infty = 1$, PIV data indicate that the recirculation regime ends at around $\mu^* = 0.66$ (see Table 2; Fig. 11). Although, the purpose of the current experiment was not to investigate performance aspects of ground effect, the distinctive change of trim required for forward flight coincides with a transition in the ground effect flow regime, and when this occurs has been shown to be highly sensitive to how the

ground is represented in the experiment. The stationary ground case shows the recirculation regime extending to higher μ^*, and the same change of cyclic trim behaviour is at correspondingly higher μ^*.

4.5 Vorticity structure IGE wake

The difference in wake structure between the ground stationary and ground moving tests highlights some interesting features of the ground effect wake. To illustrate, these cases from the ground stationary and ground moving tests are compared, but the basis for comparison is that the separation point is at the same location. Cases for the mean-flow topological separation point at $1.7R$ are discussed; Fig. 6 frame (c) at $\mu^* = 0.76$ shows mean-flow vorticity for the ground stationary case, and Fig. 15 frame (a) shows mean vorticity at $\mu^* = 0.62$ for $V_g/V_\infty = 1$. Both these cases are in the recirculation regime. The significant difference in the mean-flow vorticity is the structure. For ground stationary, the maximum positive vorticity is at the centre of the recirculation zone, while for the ground moving the maximum positive vorticity is towards the edge. The moving ground case also suggests that the recirculation zone is longer and extends to a greater height, and Table 3 shows details of the recirculation zone characteristics in which it can be seen that the enstrophy dispersion radius is larger for the ground moving case. Comparison of the two cases discussed here indicates that
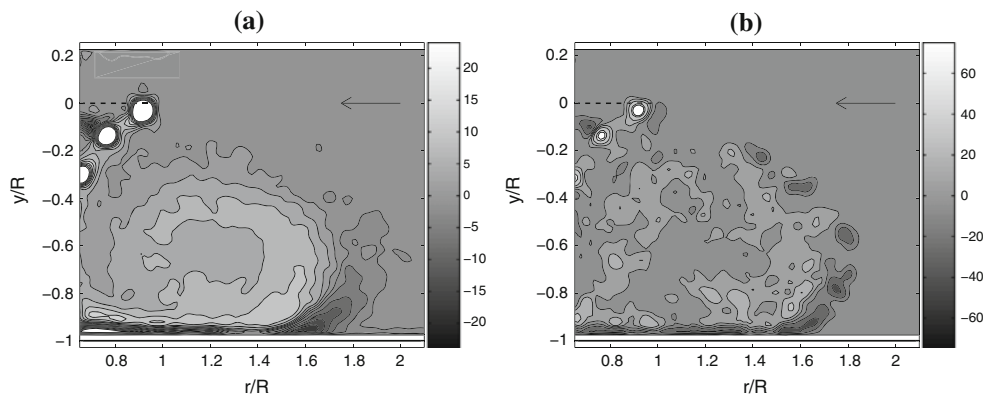

Fig. 15 Non-dimensional vorticity in the ground effect wake for the rotor at height $h/D = 0.5$ *above* the ground, rotor trimmed, moving ground $V_g/V_\infty = 1$ and $\mu^* = 0.62$. The mean-flow topological separation point is at $r/R \approx 1.7$. **a** is for mean-flow vorticity, **b** is a typical vorticity snapshot. The rotor disk is shown by the *black, horizontal line*, and the direction of the wind tunnel flow from *right to left* is shown on the vorticity *plots*. **a** Mean-flow vorticity. **b** Vorticity snapshot

Table 3 Effect of moving ground on vorticity centroid location and enstrophy dispersion radius for mean-flow topological separation point at $r/R = 1.7$

μ^*	Ground speed	Separation location (R)	Vorticity centroid (r, y) [R]	Enstrophy dispersion radius (R)
0.62	$V_g/V_\infty = 1$	1.7	(1.30, −0.73)	0.46
0.76	$V_g/V_\infty = 0$	1.7	(1.33, −0.75)	0.39

for ground moving the integrated negative vorticity is almost twice that observed in the ground stationary case. This alone would make the enstrophy dispersion radius larger, but the distribution of positive vorticity is also more diffuse than for the ground stationary case.

Trailed vortices travel down from the rotor tip, pass underneath the recirculating flow zone and travel upstream over the ground. Negative vorticity is the result of interaction of the passage of these trailed vortices over the ground and is not believed to come from the negative vorticity trailed from the blade root region. Flow visualisation of a rotor in forward flight ground effect showed how the recirculation zone interacted with these trailed vortices (Nathan and Green 2009), which are also observed to induce local secondary separation as they pass over the ground. Velocity gradients are higher in the moving ground, case, and therefore the negative vorticity is expected to be stronger and secondary separation is more likely. Individual snapshots suggest that the strength of these negative vorticity filaments is sufficient for them to pair with positive vorticity (remnants of trailed vortices), and the strong induction effect by the negative vorticity causes the positive vorticity clumps to remain in a more outboard location. A typical instantaneous flow snapshot is presented in Fig. 15 frame (b) for the ground moving case, and strong, negative vorticity filaments are seen at the periphery of the recirculation zone close to the majority of the positive vorticity filaments. Similar organised structures are not seen in the ground stationary case.

5 Conclusions

An investigation of flow around a model helicopter main rotor in forward flight IGE has been performed in a wind tunnel equipped with a rolling road. The structure of the wake flow was investigated using PIV in the cases of a stationary ground (hover in a cross-wind) and with the ground moving at the wind tunnel speed past the rotor, which is the more correct experimental simulation. The rotor wake flow is characterised by the rotor blade trailing vortices coalescing into a large, recirculating vortex above the ground, and the formation of this is affected by the moving ground speed. Significant differences in the position of the mean-flow separation along the ground, the size of the wake and the distribution of vorticity were observed. In the moving ground case the wake was smaller, and the vorticity was distributed away from the centroid of the recirculation zone. Furthermore, the moving ground generated strong vorticity of opposite sign to the rotor blade trailed vorticity. The major effect of the moving ground is to cause the transition from the so-called recirculation regime to ground vortex regime to occur at a much lower advance ratio, and this has significant trim implications from a rotor performance point of view .

References

Barlow J, Rae W Jr, Pope A (1999) Low-speed wind tunnel testing, 3rd edn. Wiley, NY

Betz A (1937) The ground effect on lifting propellers. In: NACA technical memorandums no. 836, Washington, DC

Boer J, Hermans C, Pengel K (2001) Helicopter ground vortex: comparison of numerical predictions with wind tunnel measurements. In: 27th European rotorcraft forum, Moscow

Boyd E, Kusmarwanto I (1983) Ground effect on a rotor wake. In: College of aeronautics report 8323. Cranfield Institute of Technology, Cranfield

Chen A, Jacob J, Savaş O (1999) Dynamics of corotating vortex pairs in the wakes of flapped airfoils. J Fluid Mech 382:155–193

Curtiss HCJ, Sun M, Putman WF, Hanker EJJ (1984) Rotor aerodynamics in ground effect at low advance ratios. J Am Helicopter Soc 29(1):48–55

Curtiss HCJ, Erdman W, Sun M (1987) Ground effect aerodynamics. Vertica 11(1–2):29–42

DaVis (2007) DaVis 7.2 Software: product manual. LaVision GmbH, Germany

Fradenburgh EA (1960) The helicopter and the ground effect machine. J Am Helicopter Soc 5(4):24

Ganesh B (2006) Unsteady aerodynamics of rotorcraft at low advance ratios in ground effect. Ph.D. thesis, Georgia Institute of Technology, Atlanta

Ganesh BA, Komerath N (2004) Unsteady aerodynamics of rotorcraft in ground effect. In: 22nd applied aerodynamics conference and exhibit, providence, Rhode Island

Ganesh BA, Komerath N (2006) Study of ground vortex structure of rotorcraft in ground effect at low advance ratios. In: 24th applied aerodynamics conference, San Francisco

Ganesh BA, Komerath N, Pulla D, Conlisk A (2005) Unsteady aerodynamics of rotorcraft in ground effect. In: 43rd aerospace sciences meeting and exhibit, Reno

Hanker E Jr, Smith R (1985) Parameters affecting helicopter interactional aerodynamics in ground effect. J Am Helicopter Soc 30(1):52–61

Hayden J (1976) The effect of the ground on helicopter hovering power required. In: 32nd annual forum of the American helicopter society, Washington, DC

Key D (1999) Analysis of army helicopter pilot error mishap data and the implications for handling qualities. In: 25th European rotorcraft forum, Rome

Knight M, Hefner R (1937) Static thrust analysis of the lifting airscrew. In: NACA technical notes no. 625, Washington, DC

Küssner H (1937) Helicopter problems. In: NACA technical memorandums no. 827, Washington, DC

Lee T, Leishman J, Ramasamy M (2008) Fluid dynamics of interacting blade tip vortices with a ground plane. In: 64th annual forum of the American helicopter society, Montréal

Leishman J (2006) Principles of helicopter aerodynamics, 2nd edn. Cambridge aerospace series. Cambridge University Press, Cambridge

Light J (1989) Tip vortex geometry of a hovering helicopter rotor in ground effect. In: 45th annual forum of the American helicopter society, Boston

Nathan N, Green R (2009) Flow visualisation of the helicopter brown-out phenomenon. Aeronaut J 113(1145):467–478

Prouty R (1985) Helicopter aerodynamics. PJS Publications, Peoria

Raffel M, Willert C, Kompenhans J (1998) Particle image velocimetry. A practical guide. Springer, Berlin

Raffel M, Richard H, Ehrenfried K, van der Wal B, Burley C, Beaumier P, McAlister K, Pengel K (2004) Recording and evaluation methods of piv investigations on a helicopter rotor model. Exp Fluids 36(1):146–156

Raffel M, de Gregorio F, de Groot K, Schneider O, Sheng W, Gibertini G, Seraudie A (2011) On the generation of a helicopter aerodynamic database. Aeronaut J 115(1164):103–112

Saijo T, Ganesh B, Huang A, Komerath N (2003) Development of unsteadiness in a rotor wake in ground effect. In: 21st AIAA applied aerodynamics conference, Orlando

Saritas M, Tinar E, Cetiner O (2004) Interaction of rotor blade tip vortices with surface. In: 11th international symposium on flow visualisation, Notre Dame

Sheridan PF, Wiesner W (1977) Aerodynamics of helicopter flight near the ground. In: 33rd annual forum of the American helicopter society, Washington, DC

Turner T (1966) Endless belt technique for ground simulation. In: Conference on v/stol and stol aircraft, NASA SP-116, Washington, DC

Turner T (1967) A moving belt ground plane for wind tunnel ground simulation and results for two jet flap configurations. In: NASA technical note TN D-4228, Hampton

van der Wall B, Richard H (2006) Analysis methodology for 3c-piv data of rotary wing vortices. Exp Fluids 40:798–812

Zbrozek J (1947) Ground effect on the lifting rotor. British ARC, R&M no. 2347